

# Controlled Synthesis and Exploration of $\text{Cu}_x\text{FeS}_4$ Bornite Nanocrystals

Joshua C. Kays, Carl R. Conti III, Artemis Margaronis, Jason E. Kuszynski, Geoffrey F. Strouse, and Allison M. Dennis\*



Cite This: *Chem. Mater.* 2021, 33, 7408–7416



Read Online

ACCESS |



Metrics & More



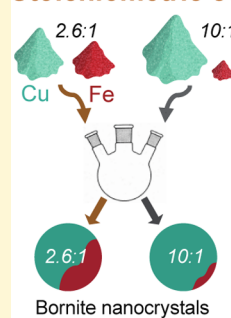
Article Recommendations



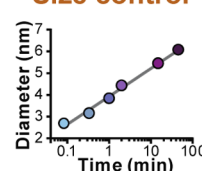
Supporting Information

**ABSTRACT:** Plasmonic semiconductor nanocrystals (NCs) are a new and exciting class of materials that enable higher control of their localized surface plasmon resonance (LSPR) than metallic counterparts. Additionally, earth-abundant and non-toxic materials such as copper iron sulfides are gaining interest as alternatives to heavy metal-based semiconductor materials. Colloidal bornite ( $\text{Cu}_5\text{FeS}_4$ ) is an interesting but underexplored example of a heavy metal-free plasmonic semiconductor. This report details the hot-injection synthesis of bornite yielding NCs ranging from 2.7 to 6.1 nm in diameter with stoichiometric control of the copper and iron content. The absorbance spectra of bornite NCs with different Cu:Fe ratios change at different rates as the particles oxidize and develop LSPR in the near-infrared region. X-ray photoelectron spectroscopy results indicate that oxidation produces sulfates rather than metal oxides as well as a decrease in the iron content within the NCs. Additionally, increasing iron content leads to decreases in carrier density and effective mass of the carrier, as determined by the Drude model. This controlled synthesis, combined with a further understanding of the relationship between the particle structure and optical properties, will enable the continued development and application of these fascinating heavy metal-free plasmonic semiconductor nanoparticles.

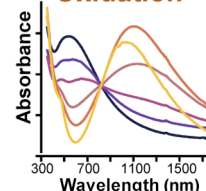
## Stoichiometric control



## Size control



## Oxidation



## INTRODUCTION

In the past 10 years, there has been increasing interest in plasmonic semiconductor nanocrystals (NCs). Unlike metallic plasmonic nanoparticles (e.g., Au, Ag) with fixed carrier densities at a given size and shape, plasmonic NCs have dynamic free carrier densities that can be modulated by intrinsic or extrinsic doping, crystal phase transitions, and even temperature.<sup>1–3</sup> This modulation changes the localized surface plasmon resonance (LSPR) peak from visible (for high carrier densities,  $10^{23} \text{ cm}^{-3}$ ) to mid-infrared (MIR) ( $10^{20} \text{ cm}^{-3}$ ) or even theoretically THz ( $10^{16}$  to  $10^{19} \text{ cm}^{-3}$ ) regimes.<sup>1</sup> Many semiconductor NCs have been explored for plasmonics, including copper chalcogenides, metal oxides (ZnO, ITO, CdO), metal nitrides (TiN, InN), and doped silicon (B:Si).<sup>3</sup> Of particular note are NCs with near-infrared (NIR) LSPRs, which are ideal for biological applications due to the increased penetration and decreased scattering of tissues at these wavelengths.<sup>4</sup> In contrast to metallic nanomaterials, semiconductor NCs can exhibit NIR LSPRs at ultrasmall sizes: indeed, the smallest gold nanorods with NIR plasmons have lengths around 50 nm,<sup>5</sup> while equivalent NIR semiconductor NCs are often a full order of magnitude smaller.<sup>3,6</sup> As a whole, the ability to dynamically control the LSPR peak position

opens doors to exciting applications in optical gating, sensing, and other optoelectronic devices.<sup>3,7</sup>

There is also a push toward using non-heavy-metal-containing compositions in semiconducting nanomaterials.<sup>8,9</sup> Recent reports of InP-based quantum dots with photoluminescent near-unity quantum yields demonstrate a competitive alternative to CdSe-based electronics.<sup>10</sup> In the solar cell field, there is active research on reducing lead and other heavy metals from perovskites.<sup>11</sup> Copper iron sulfides are attractive earth-abundant alternatives due to their low cost, useful band gaps between 0.5 and 1.25 eV, and non-toxicity. Bornite ( $\text{Cu}_5\text{FeS}_4$ ) is particularly interesting due to its potential (but unproven) direct band gap;<sup>12,13</sup> however, there have been conflicting reports on the optical properties of bornite, potentially because the material susceptibility to oxidation confounds investigations into the structure–function relationship. Some studies report bornite absorbances similar

Received: June 12, 2021

Revised: August 20, 2021

Published: September 8, 2021



to those of copper sulfides (with large infrared LSPRs), including one report claiming tunability of the LSPR with Cu:Fe ratio,<sup>14</sup> while others showed absorbance with supposedly direct band gap behavior<sup>13</sup> or a mix of both.<sup>15</sup> A recent report elaborates on the optical properties of bornite by demonstrating that increasing iron content in bornite causes a resonance at 500 nm (similar to chalcopyrite) and oxidation leads to the infrared LSPR at  $\sim 1000$  nm *via* iron leaching.<sup>16</sup> The report focused on particles  $\sim 15$  nm in diameter with significantly less efficient incorporation of iron than copper (14–20%), rendering stoichiometric control of the NC composition challenging.

We devised a synthetic protocol that yields small particle sizes (diameters from 2.7 to 6.1 nm) and controllable copper to iron ratios with near equal cation incorporation efficiencies, enabling stoichiometric control. We examine the oxidation-dependent development of the LSPR over time and experimentally determine the carrier density of oxidized NCs with different copper to iron ratios, comparing the results to fits with the Drude model. Finally, we confirm the oxidation mechanism of Lee, *et al.*<sup>16</sup> and extend these findings with X-ray photoemission spectroscopy (XPS) data to examine the structural changes taking place with the expulsion of iron from the NCs.

## ■ EXPERIMENTAL SECTION

**Materials.** Copper (II) acetylacetonate ( $\text{Cu}(\text{acac})_2$ , 97%), iron (III) acetylacetonate ( $\text{Fe}(\text{acac})_3$ ,  $\geq 99.9\%$ ), 1-dodecanethiol (DDT,  $\geq 98\%$ ), oleic acid (OA, technical grade, 90%), oleylamine (Olam, technical grade, 70%), toluene (anhydrous), nitric acid (70%, TraceMetal grade), and tetrachloroethylene (TCE,  $\geq 99.9\%$ ) were purchased from Sigma-Aldrich. Hexanes (Optima for HPLC,  $\geq 99.9\%$ ), isopropyl alcohol (99.5%), ethanol (anhydrous, histological), and cobaltocene (98%) were purchased from Fisher Scientific, while sulfur (refined, 99.5%) was procured from ACROS Organics. Quartz glass cuvettes were sourced from Starna Cells Inc. Gold nanorods (10 nm  $\times$  67 nm), citrate-coated, were purchased from Nanopartz, and 1,2-distearoyl-*sn*-glycero-3-phosphoethanolamine-*N*-[methoxy-(polyethylene glycol)-2000] (ammonium salt) was purchased from Avanti Lipids. All air-sensitive materials were stored and handled in a glovebox under an argon atmosphere.

**Methods. Synthesis of Bornite.** Bornite NCs were synthesized by hot injection. A total of 1.2 mmol of  $\text{Cu}(\text{acac})_2$  and  $\text{Fe}(\text{acac})_3$  (at Cu/Fe ratios from 10:1 to 2.6:1 Cu/Fe) and 6.7 mL of OA were loaded to a 100 mL round-bottom flask with a stirbar in an argon-filled glovebox. The flask was attached to a Schlenk line and heated to 105 °C under vacuum to degas. The flask was flushed with argon and heated to 150 °C to dissolve all metal salts and then heated to 180 °C. In a separate flask, 0.2 M sulfur in oleylamine (S/Olam) was heated to 90 °C under argon. When the reaction flask reached 180 °C, 1.5 mL of DDT was injected causing the solution to turn dark yellow. After  $\sim 30$  s to allow the temperature to recover, 15 mL of S/Olam (total 3 mmol sulfur) was added dropwise over 5 min, followed by 5 min annealing at 180 °C. Once cooled to room temperature, the reaction solution was transferred into the glovebox. We note that these reactions turn solid upon cooling below  $\sim 40$  °C.

In a modified reaction, the same reagents run at half the scale (0.6 mmol cations) were added to a six-dram vial in the glovebox and heated to 180 °C on a thermostated hot plate with an aluminum heating block for vials. The reaction was carried out as described above, except that S/Olam was injected as a bolus, followed by sampling at various time points.

**Precipitation and Cleaning of NCs.** NCs from the reaction solution were added to hexanes at a 1:1 ratio (volume) and centrifuged at 21,000 rcf for 2 min to remove precipitates. The pellet was discarded, and the supernatant containing the NCs was transferred to a new tube for precipitation with ethanol.

Centrifugation at 21,000 rcf for 5 min deposited the NC precipitates on the sides and bottom of the tube. The supernatant was discarded, and the pellet was washed with 1 mL of isopropyl alcohol to fully remove excess ligands before the NCs were suspended in the solvent of choice (hexanes, carbon tetrachloride, etc.).

**Powder X-ray Diffraction.** X-ray diffraction (XRD) was performed on a low-background silicon substrate. Twice cleaned NCs suspended in carbon tetrachloride or hexanes were drop-cast on the silicon substrate, and the resulting pellet was rinsed with ethanol to remove excess ligands. Measurements were taken on a Bruker D2 Discovery system in the powder diffraction mode using Cu K $\alpha$  radiation with a 2.5° soller filter set. Detection occurred with 0.4–1.0 s integration times per step at  $\sim 0.03^\circ$  steps, and spectra were background-subtracted and exported for analysis. Data analysis was conducted with Fityk software for peak fitting.

**Transmission Electron Microscopy.** Transmission electron microscopy (TEM) images were taken on a JEOL ARM 200F. Samples were prepared by drop-casting dilute solutions of twice cleaned NCs in toluene onto nickel TEM grids (Electron Microscopy Services, 400 mesh). The grid was cleaned with ethanol and dried at 40 °C in a vacuum oven for 10 min or dried in the glovebox under ambient conditions. Samples were stored under argon until imaging to minimize oxidation.

**X-ray Photoemission Spectroscopy.** XPS scans were taken on a Thermo Scientific K-Alpha+ XPS in the constant analyzer energy mode with a 0.1 eV step size and averaged across 10 scans. Samples were drop-cast onto a silicon substrate in an identical manner to XRD experiments. All scans were corrected to the adventitious carbon binding energy (B.E.) peak at 284.8 eV. Peaks were fit with Pseudo-Voigt functions (typically 0.3–0.5, with a consistent shape across all peaks in a scan). For iron and sulfur, additional constraints were placed on the multiplet and the  $2p^{1/2}$  peak position and area relative to the main  $2p^{3/2}$  peak, in accordance with reference spectra.

**Elemental Analysis.** To determine iron and copper content in NCs, microwave plasma atomic emission spectroscopy (MP-AES) was performed on an Agilent 4200 instrument. In general, samples were precipitated as described above and suspended in a volatile solvent for transfer to an acid-cleaned glass vial. After evaporation, the dried NCs were dissolved completely (digested) by trace-metal grade nitric acid and diluted to 5% acid with ultrapure water. Each sample had quadruplicate instrument runs, and concentrations were determined using a matrix-matched standard curve of iron and copper run concurrently with the samples.

**Absorbance and Oxidation Experiment.** All absorbance measurements were performed on a CARY5000 UV/Vis/NIR spectrophotometer. Unoxidized samples were cleaned within an argon glovebox, resuspended in nitrogen-packed TCE, and transferred to a dried, sealable quartz cuvette. For the oxidation experiments,  $\sim 1.5$  mL of sample was stored in a sealed glass one-dram vial and agitated continuously at 60 RPM on the reciprocating shaking setting. At given time points, the sample was transferred to a quartz cuvette for absorbance measurements.

**Titration with the Single-Electron Reductant.** Cobaltocene was dissolved into anhydrous toluene (10 mM) in the glovebox. Aliquots of 0.1–30  $\mu\text{L}$  of cobaltocene were titrated into 1 mL aliquots of oxidized NCs in toluene; after 30 min, samples were transferred to a capped semimicro quartz cuvette for absorbance measurements. Absorbance spectra were integrated and plotted against cobaltocene amounts to determine the carrier density.

**Photothermal Demonstration.** 1 mL of 27  $\mu\text{g}/\text{mL}$  of either oxidized CFS-7:1 or gold NRs was added to a 3 mL quartz cuvette with a 1/8 inch diameter temperature probe inserted midway. The sample was illuminated with a 0.7 W output power 1050 nm LED from Ushio, positioned  $\sim 3$  mm away, and temperatures were recorded every 20–30 s. After 20 min, the LED was turned off, and samples were cooled naturally.

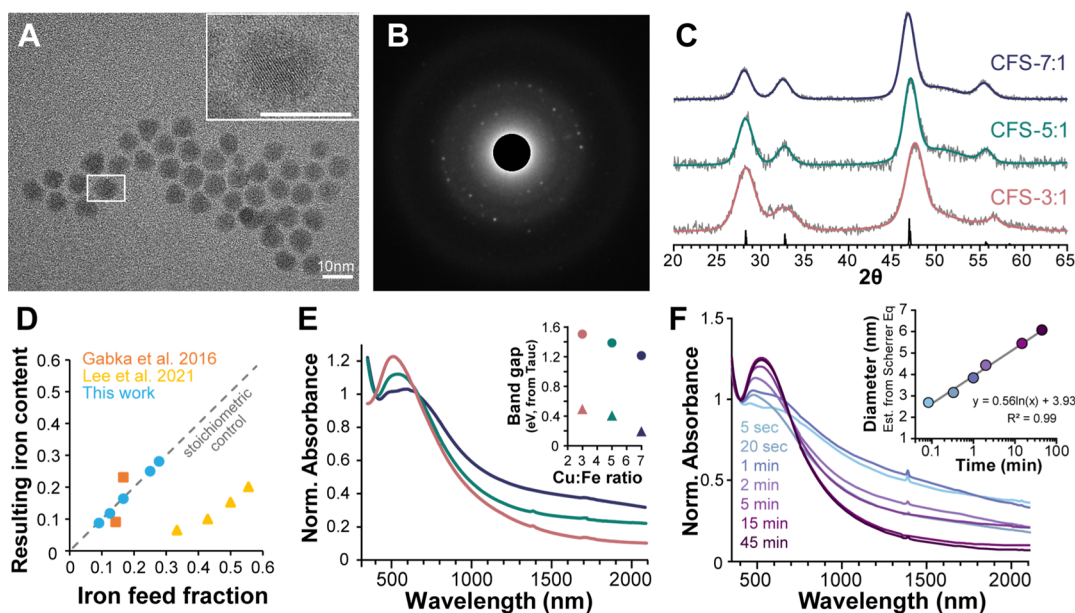


**Figure 1.** Structural, chemical, and optical characterization of bornite NCs. (A) Representative TEM of CFS-5:1 NCs, with sizing in the [Supporting Information](#) (Figure S2). The inset (white box) is a higher magnification image showing lattice fringes. Both scale bars are 10 nm. (B) SAED image from bornite NCs. (C) XRD profiles of different bornite NCs drop-cast on the substrate, along with the bornite American Mineralogist Crystal Structure Database standard (AMCSD 0000048) in black. (D) Iron content of NCs compared to feed ratio, demonstrating stoichiometric control. Data included from refs [15](#) and [16](#). (E) Absorbance of unoxidized bornite NCs normalized to 400 nm, with the inset of band gaps (indirect = triangles, direct = circles) calculated from Tauc plots ([Figure S4](#)). (F) Absorbance of unoxidized time points drawn from CFS-5:1 synthesis, normalized to 400 nm. The inset shows estimated diameter from XRD (*via* the Scherrer Equation) plotted against reaction time, along with a logarithmic fit.

## RESULTS AND DISCUSSION

Bornite NCs with various copper to iron ratios were synthesized by hot injection under air-free conditions. Briefly, copper (II) acetylacetonate and iron (III) acetylacetonate were dissolved in OA. After heating to 180 °C, 1.5 mL of DDT was injected, followed by a drip injection of S/Olam. We found that both anions (DDT and S/Olam) are necessary for phase-pure synthesis of bornite: using DDT alone produced insoluble NCs of an indistinguishable phase, while reactions using only S/Olam yielded covellite copper sulfide ([Figure S1](#)).

The crystallinity was seen in TEM and selected area electron diffraction (SAED) images of bornite NCs ([Figure 1A–C](#)) that correlate with XRD measurements of the same samples. The sizes of all three Cu:Fe ratio NCs were similar, although CFS-3:1 was slightly smaller (5.5 nm) than CFS-5:1 and CFS-7:1 (7.1 and 6.6 nm, respectively, see [Figure S2](#)). Increases in the iron content led to small, monotonic increases in the  $2\theta$  position across all peaks, consistent with a dose-dependent decrease in *d* spacing ([Table S1](#)).<sup>16</sup> This indicates a mild contraction of the crystal lattice, most likely due to the higher electronegativity of  $\text{Fe}^{3+}$  relative to  $\text{Cu}^{1+}$ . MP-AES analysis of cleaned NCs showed remarkably tight control of iron incorporation: the feed ratio to measured ratio of Cu:Fe was between 94 and 100% for all samples, including both very low and very high Fe content samples, that is, CFS-10:1 and a CFS-2.6:1, respectively ([Figure 1D](#)). The CFS-2.6:1 sample is the lowest ratio (i.e., the highest iron content at 28.1% Fe of cations by mole) bornite synthesized to date to the authors' knowledge, and it retained a pure bornite crystal structure ([Figure S3](#)). Notably, increasing iron feed ratio (Cu/Fe 2:1, 1.5:1, etc.) led to the formation of  $\text{CuFeS}_2$  chalcopyrite phase NCs; diluting the 5:1 Cu:Fe feed ratio reaction concentration 10-fold also led to chalcopyrite NCs (data not shown). These

data imply that the chalcopyrite phase is more favorable thermodynamically and that these specific synthetic conditions are needed to kinetically trap the bornite phase.

As the iron content in the NCs increases, an increasingly pronounced and more symmetric absorbance feature emerges around 500 nm, similar to the spectra of chalcopyrite NCs. Furthermore, increasing the iron content increases the band gap, as determined by Tauc plots ([Figure 1E](#) inset, [Figure S4](#)). Notably, low-iron-content bornite—even down to 10:1 Cu:Fe—retained bornite-like absorbance ([Figure S5](#)), in contrast to the most recent work.<sup>16</sup> Differences in the synthetic approach or handling could explain this discrepancy. Copper-heavy bornite appears to have a more metallic absorbance, with a long tail that did not reach zero even out to 2500 nm (the limit of our instrument), while iron-heavy bornite exhibited less of an absorbance tail.

To examine the impact of size on absorbance and to improve the size dispersion of the particles, a modified synthesis of CFS-5:1 was performed entirely in the glovebox, allowing for rapid sampling at early time points without oxidation. This procedure also used a rapid bolus injection of the S/Olam precursor instead of a continuous drip addition over 5 min. Samples were cleaned twice in the glovebox to remove excess ligands and suspended in argon-flushed TCE for absorbance measurements or drop-cast on silicon substrates for XRD characterization and TEM examination. This synthesis enabled tight control of the size with diameters determined from XRD ranging from 2.7 to 6.1 nm ([Figure 1F](#) inset, [Figure S6](#)), values that matched well with TEM analysis ([Figure S7](#)). We found that the absorbance feature at ~500 nm developed with increasing size, while smaller sizes (4 nm or less) appeared to lack this feature ([Figure 1F](#)). Elemental analysis performed on multiple time points in the synthesis showed no



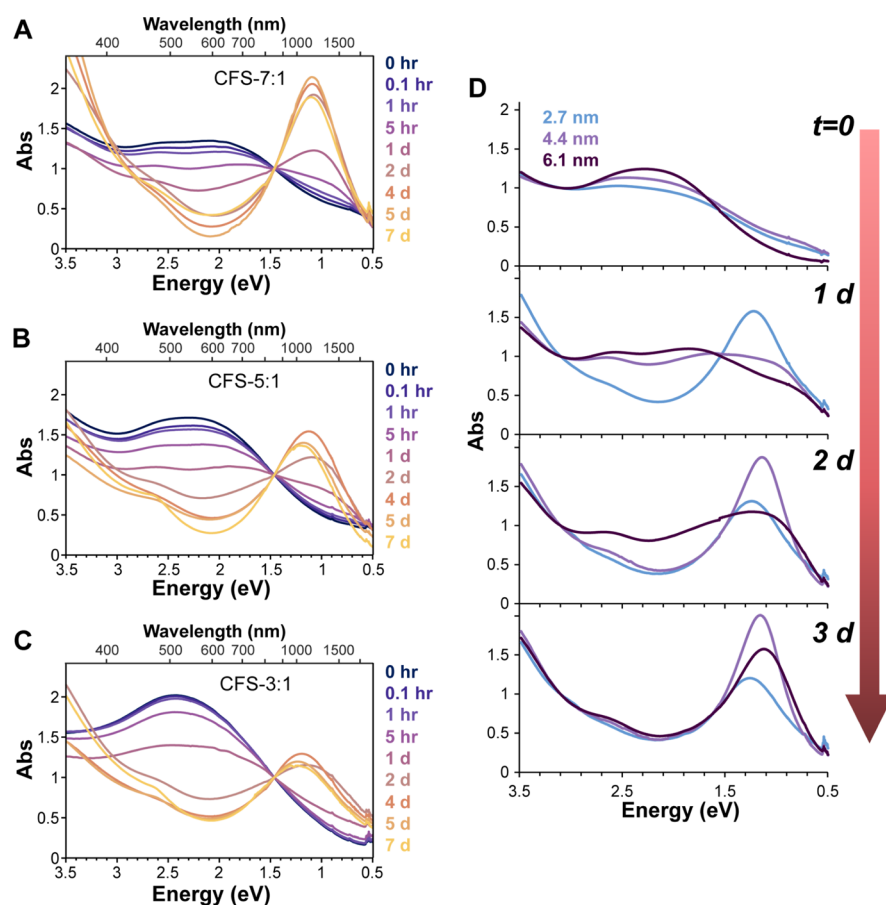


**Figure 2.** Oxidation of Bornite NCs. Oxidation of CFS-7:1 (A), CFS-5:1 (B), and CFS-3:1 (C) bornite NCs over time. All curves normalized to 1.5 eV, which was the position of a near isosbestic point in the raw data. (D) Oxidation of CFS-5:1 NCs of different sizes over time.

significant trend or variation in the copper to iron ratio (Figure S8), ruling out time-dependent compositional changes as the source of the LSPR peak at 500 nm. The emergence of LSPR at larger sizes appears to indicate confinement of the carrier (in this case, electrons) as a decrease in NC radius increases the confinement energy ( $E_{\text{confinement}} \propto \frac{1}{r^2}$ ) while also decreasing the Coulomb repulsion energy ( $E_{\text{Coulomb}} \propto r^2$ ) for a carrier at the surface of the NC. Thus, at small sizes, the confinement energy is much greater than the surface Coulomb repulsion and LSPR cannot exist, while at larger sizes, the confinement energy decreases (and the Coulomb repulsion energy increases) rapidly, enabling the collective resonance to emerge.<sup>17</sup>

While handling bornite samples outside of the glovebox, we noticed surprising color changes over time or with repeated precipitation-based cleaning: samples turned from a dark-black or purple to a pale-greenish color with a far lower optical density by eye. We systematically examined this change in the presence of air by measuring the absorbance in TCE at various time points while solutions were agitated under ambient conditions. All samples exhibited time-dependent changes in absorbance upon exposure to air.

The copper to iron ratio influenced the oxidation rate: CFS-7:1 showed rapid changes in absorbance in the first few hours and the development of an infrared peak at  $\sim 1.1$  eV ( $\sim 1100$  nm) by 1 day, while this peak did not develop until day 2 for CFS-5:1 and CFS-3:1. All samples appear to follow roughly first-order kinetics in change until reaching a relative plateau by

2–4 days (Figure S9), implying that a single process drives the optical changes. However, CFS-7:1 and CFS-5:1 show a faster non-linearity at the first few time points, which may indicate a secondary initial process.

Remarkably, the final LSPR peak position did not dramatically change with increasing iron content, yielding a slight blue shift (1.1, 1.2, and 1.25 eV) with increasing Fe content. This was initially surprising as doping or alloying copper chalcogenides with tertiary or quaternary ions leads to a progressive decrease and red shifting of the LSPR peak<sup>18,19</sup> via filling of the excess holes. As recently shown, LSPR development can also coincide with significant iron leaching,<sup>16</sup> which we confirmed *via* MP-AES. Interestingly, high-Fe-content bornite showed less loss of Fe, with a drop of only 30% in iron content for CFS-3:1 relative to its initial state relative to 60 and 95% drops for CFS-5:1 and CFS-7:1 bornite samples, respectively (Figure S10). This makes oxidized bornite distinct from copper sulfide in both the composition and mechanism of LSPR formation: significant iron remains in the high-Fe-content bornite after oxidation, and LSPR arises from the leaching of Fe ions and not the loss of Cu as in copper chalcogenides.

We also examined how size impacts the change in optical properties due to oxidation over time. The absorbance spectra of three sizes of CFS-5:1 were recorded several times following exposure to ambient air (Figure 2D; spectra of unoxidized samples in Figure 1F). There was a clear trend in oxidation rate and size as the smallest bornite NC (2.7 nm) showed an LSPR peak by day 1, the next size (4.4 nm) exhibited LSPR by

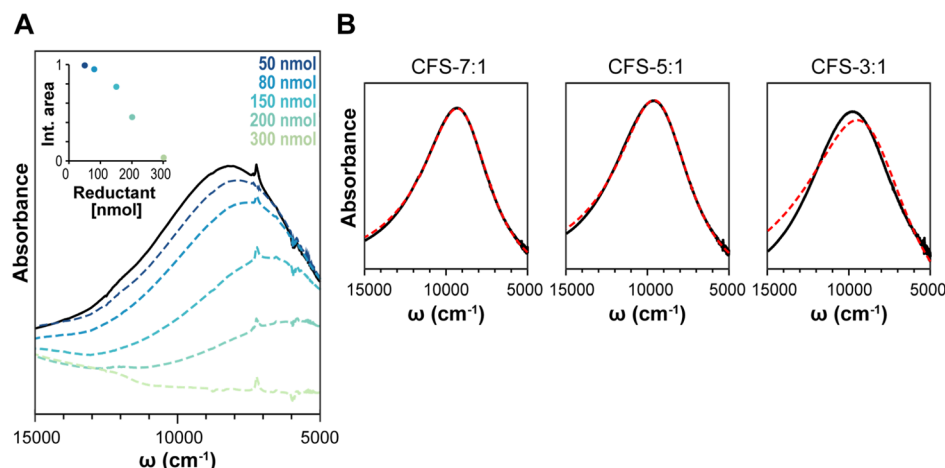


**Figure 3.** (A) Titration of CFS<sub>ox</sub> 5:1 with the cobaltocene reductant. The inset is the integrated plasmon area at different titrations. (B) Frequency-independent Drude fits for various bornite samples. Experimental data were fit using the MATLAB code from ref 21.

day 2, and the largest (6.1 nm) by day 3. This indicates that the oxidation is surface-limited: the higher the surface area/volume ratio, the faster the oxidation occurs. In all three sizes of CFS-5:1, the loss of electrons through oxidation results in excess hole carriers that produce p-type LSPR in the NIR; in contrast, only the larger particles exhibit a resonance feature at 500 nm pre-oxidation (Figure 1F). These observations indicate that the electron-based resonance at 500 nm is more impacted by size-based confinement than the hole-based NIR LSPR. Thus, at a given size, the electron would be more confined than the hole, causing confinement effects to dominate (i.e.,  $E_{\text{confinement}} \gg E_{\text{Coulomb}}$ ). In this context, the hole for bornite must be heavier than the electron since confinement energy is inversely proportional to the effective mass ( $E_{\text{confinement}} \propto \frac{1}{m_{\text{effective}}}$ ).<sup>17</sup>

The LSPR of each sample was fit using the simple Drude model to examine the effect of Cu:Fe ratio on the effective mass as well as on the overall dampening of the plasmon resonance (see the Supporting Information note for methods). The literature value for the dielectric constant of Cu<sub>5</sub>FeS<sub>4</sub> (3.48) and the frequency-independent Drude model were used for these fits.<sup>20,21</sup> Since the effective mass of the carriers in these materials remains largely uncertain, one-electron reductant chemical titrations were performed (Figure 3A) to independently measure the free carrier density, enabling use of the Drude model to calculate  $m^*$  for each sample. Determining the free carrier concentration independent of the Drude model is critical toward understanding the properties of plasmonic semiconductors as the Drude model has previously been shown to be inaccurate when calculating the carrier density from the LSPR extinction feature alone.<sup>22–25</sup> The Drude model- and chemical titration-extracted parameters are listed in Table 1, while the frequency-independent fits are shown in Figure 3B.

The similar frequency of each LSPR results in consistent values for the plasma frequency ( $\omega_p$ ) for all Cu:Fe ratios. A trend begins to emerge once the damping constant ( $\Gamma$ ) for each sample is examined.  $\Gamma$  is a measure of the overall scattering function for the material and is related to the line width and lifetime of the LSPR.<sup>26</sup> Drude fitting of the NIR extinction feature reveals that  $\Gamma$  increases as the Cu:Fe ratio decreases, indicating an increased scattering mechanism for

**Table 1.** Drude Model- and Chemical Titration-Calculated LSPR Parameters

sample	$\omega_{\text{LSPR}}$ (cm <sup>-1</sup> )	$\omega_p$ (cm <sup>-1</sup> )	$\Gamma$ (cm <sup>-3</sup> )	titration $n/10^{21}$ (cm <sup>-3</sup> )	Drude $m^*$
CFS <sub>ox</sub> -7:1	9312	26,390.1	5051.31	12.6	1.63 $m_e$
CFS <sub>ox</sub> -5:1	9616	27,262.9	5484.71	10.6	1.28 $m_e$
CFS <sub>ox</sub> -3:1	9748	26,842.4	7490.16	8.51	1.03 $m_e$

samples with higher relative concentrations of Fe. Since both the titration-measured carrier densities and Drude-calculated  $m^*$  decrease from the CFS-7:1 sample to CFS-3:1 sample, the primary scattering mechanism cannot arise from hole–hole or hole–phonon interactions. The similar sizes of each sample (5.5–7 nm) also rule out surface scattering as a significant contributor to the observed change in  $\Gamma$ . This leaves the two most likely sources of the increased damping to be defect and interband scattering. Increased defect scattering can result from a larger number of metal and oxygen vacancies formed during the oxidation process, while interband scattering may be a result of higher Fe 3d orbital contributions within the band gap with higher relative concentrations of Fe.

It is also important to note the better fits observed for the CFS<sub>ox</sub>-7:1 and CFS<sub>ox</sub>-5:1 samples compared to the CFS<sub>ox</sub>-3:1. The excellent fit using the frequency-independent Drude model indicates that vacancies may be more effectively screened in the higher Cu:Fe samples, leading to frequency-independent damping. These data suggest that these samples might have a higher dielectric constant than the CFS<sub>ox</sub>-3:1 sample. Cu<sub>1.85</sub>Se has been known to exhibit frequency-independent damping by screening Cu vacancies due to its high dielectric background ( $\epsilon_{\infty} = 10$ ).<sup>27</sup> Further investigations into the electronic band structure, scattering mechanisms, and the effective masses of these materials are currently underway.

To better understand the oxidation process that leads to the formation of LSPR, we performed XPS of CFS<sub>ox</sub>-3:1 bornite before and after oxidation (Figure 4). The copper state did not change during oxidation, while both iron and sulfur exhibited shifts in composition and oxidation state. Specifically, the sulfur spectrum showed oxidation compared to fresh samples with a loss of the S<sup>2-</sup> population corresponding to increases in S<sup>1-</sup> and S<sup>6+</sup> in the form of SO<sub>4</sub> sulfate (see the peak at 169 eV). This oxidation of sulfur mirrors studies of the single-crystal bornite ore after exposure to air<sup>28</sup> or after leaching with an

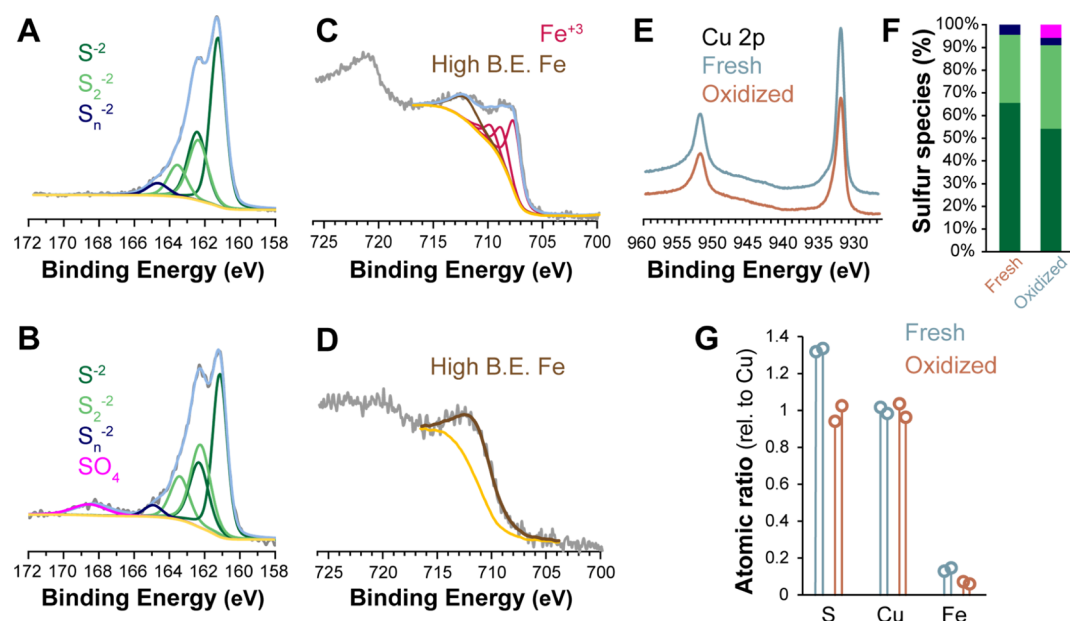


**Figure 4.** XPS of bornite NCs before and after oxidation. XPS for (A) fresh and (B) oxidized CFS-3:1 in the sulfur 2p regime as well as iron 2p spectra for (C) fresh and (D) oxidized samples. (E) Cu 2p peaks of fresh and oxidized CFS-3:1. The offset is for clarity only. (F) Sulfur quantification from spectra in (A) and (B). (G) Atomic ratio of sulfur, copper, and iron, normalized to the average copper signal per sample with two measurements per sample.

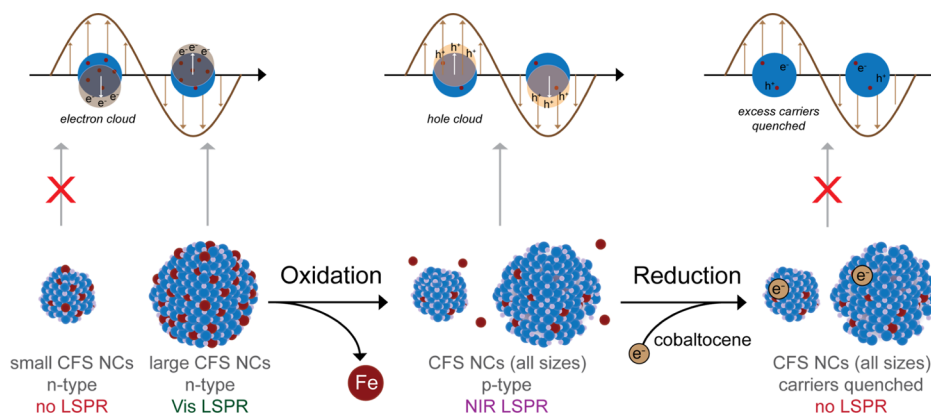


**Figure 5.** Summary schematic. Unoxidized NCs (left) are n-type doped semiconductors with a visible LSPR that can be lost with confinement effects at smaller sizes. Oxidation causes the loss of iron content (middle), leading to p-type doping and NIR LSPR arising from the excess holes for all NC sizes. Subsequent reduction of the NCs (right) by cobaltocene quenches the NIR LSPR.

alkaline (but not acidic) medium.<sup>29</sup> These oxidation data may also hint at the mechanism behind the  $\text{Fe}^{3+}$  stoichiometry in the bornite crystal structure: given the decrease in  $\text{S}^{2-}$  after iron leaching, one may expect higher  $\text{S}^{2-}$  abundance in  $\text{Fe}^{3+}$ -rich bornite to accommodate the extra positive charge.

The iron state changed significantly, with a loss of the  $\text{Fe}^{3+}$  multiplet peaks at 708–710 eV after oxidation (Figure 4C,D and S11). Both samples contain a broad, high B.E. peak that was not easily matched to reference spectra for iron sulfides. Given that iron leaches out of these NCs, it is likely that this broad peak arises from interstitial iron as its leaching. This is supported by a similar broad high-energy peak found at the surface of iron sulfides, in which  $\text{Fe}^{3+}$  ions experience a reduction in coordination as well as differences in crystal field energy.<sup>30</sup> Both these phenomena as well as changes in the electron density surrounding the  $\text{Fe}^{3+}$  ion could impact interstitial ions leaching through the crystal lattice, which explains why interstitial cations typically exhibit higher B.E.

than their lattice-bound counterparts.<sup>31</sup> One paper ascribes the broad peaks around 712 eV to an Cu LMM Auger peak (although no reference was given);<sup>32</sup> however, the  $\text{Fe}^{3+}$  peak pre-oxidation consistently matches that of natural bornite ore in the literature.<sup>28,32,33</sup> Copper did not appear to change oxidation states: the spectra showed a  $2p^{3/2}$  peak around 932.5 eV for both oxidized and fresh samples, which matches well with spectra for Cu(I) (Figure 4E). Additionally, neither spectrum contains the signature Cu(II) satellite peaks between 940 and 945 eV, further confirming that the copper in bornite is in the Cu(I) state. When looking at the quantification of the XPS results, the iron content dropped relative to copper content, down to 15.2:1 Cu:Fe compared to 7.2:1 for the fresh CFS-3:1 (Figure 4G). We note that the discrepancy between MP-AES-measured 3:1 fresh bornite and the XPS quantification of the fresh sample at 7.2:1 may be due to beam damage leading to loss of the Fe signal,<sup>34</sup> differences in the penetration depth at high versus lower B.E., or some loss of Fe during

repeated cleaning of the sample before drop-casting onto the substrate. Regardless, a consistent drop of iron content in the oxidized samples is found by both XPS and MP-AES (Figures 4G and S10). Furthermore, there was a drop in sulfur content relative to copper, which points to the potential shedding of these ions from the NC, with further exploration being warranted. Finally, XPS of oxygen (Figure S12) showed a peak around 532.0 eV for both pre- and post-oxidation samples that does not match with metal oxide or metal hydroxides and instead is consistent with S=O bonding in sulfate as well as other organically bound oxygen.

In Figure 5, we aggregate the analysis of the material properties at the various stages of synthesis, oxidation, and reduction to summarize the correlation between the material structure and optical behavior. Small particles (<4 nm diameter) synthesized using the shortest reaction times do not exhibit LSPR as the electron confinement energy is higher than the surface Coulomb repulsion. Larger particles (>4 nm diameter) of the same CFS crystal structure, however, evidence lower electron confinement and higher surface Coulomb repulsion, leading to electron-mediated plasmonic resonance ~500 nm. Oxidation of the particles is associated with leaching of the Fe ions, producing vacancies in the crystal structure and an excess of holes as electrons are removed from the material. The p-doped LSPR exhibited by these oxidized particles of all sizes and stoichiometries yields resonance in the NIR in the form of a broad absorbance peak around 1100 nm, which can be quenched by neutralizing the excess hole carriers through reduction with cobaltocene.

LSPR in the infrared is useful for multiple optoelectric and biomedical applications.<sup>35–38</sup> For example, various gold nanostructures have been used for their photothermal properties, which induces localized heating that can be used for photothermal therapy under continuous illumination<sup>39,40</sup> or photoacoustic imaging with pulsed illumination.<sup>5</sup> To demonstrate the photothermal effect of the much smaller CFS nanoparticles, we compared the ensemble heating behavior of oxidized CFS-7:1 to gold nanorods (NRs, 67 nm × 10 nm length × width) with 1064 nm LSPR peaks at equivalent mass concentrations (Figure S13). For appropriate comparison to the water-soluble, citrate-capped gold NRs, the bornite NCs were rendered water-soluble by encapsulation in a lipid-PEG micelle.<sup>41,42</sup> With no optimization of coatings or size, bornite performed equally well compared to gold nanorods in this simple experiment, with both achieving a 14 °C increase in temperature after 20 min of illumination. The use of smaller particle sizes and bioessential elements may be advantageous in biomedical applications, warranting further studies into the application of bornite CFS.

## CONCLUSIONS

In summary, we report a synthetic protocol to generate bornite NCs with a range of Cu:Fe ratios—including the highest iron incorporation to date—with near unity incorporation efficiencies. We found that increasing the iron content led to slower oxidation rates and less iron leaching during oxidation. Through chemical titration, we determined that oxidized bornite NCs with a higher iron content exhibit a lower carrier density and effective mass as well as a larger LSPR line width, indicating differences in electron scattering. Our size series also demonstrates confinement of the resonance peak at 500 nm pre-oxidation for the first time, while oxidation of these different sizes all led to p-doped LSPR in the infrared, implying

significant differences in confinement of the hole and electron. We utilize XPS to observe atomic changes due to oxidation, confirming that oxidation of bornite induces iron leaching and produces sulfates and not metal oxides. As a whole, the tight control of composition and size has enabled an exploration of how Cu:Fe ratio and size fundamentally change the optical and electronic properties of these interesting earth-abundant plasmonic NCs.

## ASSOCIATED CONTENT

### Supporting Information

The Supporting Information is available free of charge at <https://pubs.acs.org/doi/10.1021/acs.chemmater.1c02029>.

Additional XRD, absorbance, TEM, XPS, and photo-thermal data, along with a note on LSPR modeling methods (PDF)

## AUTHOR INFORMATION

### Corresponding Author

Allison M. Dennis – Department of Biomedical Engineering and Division of Materials Science & Engineering, Boston University, Boston, Massachusetts 02215, United States; [orcid.org/0000-0001-5759-9905](https://orcid.org/0000-0001-5759-9905); Email: [aldennis@bu.edu](mailto:aldennis@bu.edu)

### Authors

Joshua C. Kays – Department of Biomedical Engineering, Boston University, Boston, Massachusetts 02215, United States

Carl R. Conti III – Department of Chemistry and Biochemistry, Florida State University, Tallahassee, Florida 32306, United States

Artemis Margaronis – Department of Biomedical Engineering, Boston University, Boston, Massachusetts 02215, United States

Jason E. Kuszynski – Department of Chemistry and Biochemistry, Florida State University, Tallahassee, Florida 32306, United States

Geoffrey F. Strouse – Department of Chemistry and Biochemistry, Florida State University, Tallahassee, Florida 32306, United States; [orcid.org/0000-0003-0841-282X](https://orcid.org/0000-0003-0841-282X)

Complete contact information is available at: <https://pubs.acs.org/doi/10.1021/acs.chemmater.1c02029>

### Author Contributions

J.C.K. and A.M.D. conceived the project; J.C.K., C.R.C., G.F.S., J.E.K., and A.M.D. designed experiments. All experiments were conducted by J.C.K. (with assistance from A.M.). C.T. performed analysis of absorbance and titration measurements for Figure 3; all other analyses were performed by J.C.K. J.C.K., C.R.C., A.M.D., and G.F.S. wrote the manuscript, and all authors have given approval to the final version of the manuscript.

### Funding

Research reported in this publication was supported by the National Institute of General Medical Sciences of the National Institutes of Health under award number R21GM135849 and the National Science Foundation under DMR-1905757. Financial support for JCK was provided by Training Grant NIH/NIGMS T32 GM008764 and by the National Science Foundation Graduate Research Fellowship (NSF-GRFP) under grant no. DGE-1840990.



## Notes

The authors declare no competing financial interest.

## ■ ACKNOWLEDGMENTS

XRD data were generated in the BU MSE Core Research Facility, funded by NSF award number 1337471. This work was performed in part at Harvard University's Center for Nanoscale Systems (CNS), a member of the National Nanotechnology Coordinated Infrastructure Network (NNCI), which is supported by the National Science Foundation under NSF award no. 1541959.

## ■ REFERENCES

- (1) Luther, J. M.; Jain, P. K.; Ewers, T.; Alivisatos, A. P. Localized Surface Plasmon Resonances Arising from Free Carriers in Doped Quantum Dots. *Nat. Mater.* **2011**, *10*, 361–366.
- (2) Mattox, T. M.; Ye, X.; Manthiram, K.; Schuck, P. J.; Alivisatos, A. P.; Urban, J. J. Chemical Control of Plasmons in Metal Chalcogenide and Metal Oxide Nanostructures. *Adv. Mater.* **2015**, *27*, 5830–5837.
- (3) Agrawal, A.; Cho, S. H.; Zandi, O.; Ghosh, S.; Johns, R. W.; Milliron, D. J. Localized Surface Plasmon Resonance in Semiconductor Nanocrystals. *Chem. Rev.* **2018**, *118*, 3121–3207.
- (4) Smith, A. M.; Mancini, M. C.; Nie, S. Bioimaging: Second Window for in Vivo Imaging. *Nat. Nanotechnol.* **2009**, *4*, 710–711.
- (5) Chen, Y.-S.; Zhao, Y.; Yoon, S. J.; Gambhir, S. S.; Emelianov, S. Miniature Gold Nanorods for Photoacoustic Molecular Imaging in the Second Near-Infrared Optical Window. *Nat. Nanotechnol.* **2019**, *14*, 465–472.
- (6) Kriegel, I.; Jiang, C.; Rodríguez-Fernández, J.; Schaller, R. D.; Talapin, D. V.; Da Como, E.; Feldmann, J. Tuning the Excitonic and Plasmonic Properties of Copper Chalcogenide Nanocrystals. *J. Am. Chem. Soc.* **2012**, *134*, 1583–1590.
- (7) Blemker, M. A.; Gibbs, S. L.; Raulerson, E. K.; Milliron, D. J.; Roberts, S. T. Modulation of the Visible Absorption and Reflection Profiles of ITO Nanocrystal Thin Films by Plasmon Excitation. *ACS Photonics* **2020**, *7*, 1188–1196.
- (8) Xu, G.; Zeng, S.; Zhang, B.; Swihart, M. T.; Yong, K.-T.; Prasad, P. N. New Generation Cadmium-Free Quantum Dots for Biophotonics and Nanomedicine. *Chem. Rev.* **2016**, *116*, 12234–12327.
- (9) Kays, J. C.; Saeboe, A. M.; Toufanian, R.; Kurant, D. E.; Dennis, A. M. Shell-Free Copper Indium Sulfide Quantum Dots Induce Toxicity In Vitro and In Vivo. *Nano Lett.* **2020**, *20*, 1980–1991.
- (10) Won, Y.-H.; Cho, O.; Kim, T.; Chung, D.-Y.; Kim, T.; Chung, H.; Jang, H.; Lee, J.; Kim, D.; Jang, E. Highly Efficient and Stable InP/ZnSe/ZnS Quantum Dot Light-Emitting Diodes. *Nature* **2019**, *575*, 634–638.
- (11) Li, J.; Cao, H.-L.; Jiao, W.-B.; Wang, Q.; Wei, M.; Cantone, I.; Lü, J.; Abate, A. Biological Impact of Lead from Halide Perovskites Reveals the Risk of Introducing a Safe Threshold. *Nat. Commun.* **2020**, *11*, 1–5.
- (12) Harmer, S. L.; Pratt, A. R.; Nesbitt, H. W.; Fleet, M. E. Reconstruction of Fracture Surfaces on Bornite. *Can. Mineral.* **2005**, *43*, 1619–1630.
- (13) Wiltrout, A. M.; Freymeyer, N. J.; MacHani, T.; Rossi, D. P.; Plass, K. E. Phase-Selective Synthesis of Bornite Nanoparticles. *J. Mater. Chem.* **2011**, *21*, 19286–19292.
- (14) Yuan, L.; Hu, W.; Zhang, H.; Chen, L.; Wang, J.; Wang, Q.; Zhang, H.; Chen, L.; Wang, J. CuSFeS<sub>4</sub> Nanoparticles With Tunable Plasmon Resonances for Efficient Photothermal Therapy of Cancers. *Front. Bioeng. Biotechnol.* **2020**, *8*, 21.
- (15) Gabka, G.; Bujak, P.; Ostrowski, A.; Tomaszewski, W.; Lisowski, W.; Sobczak, J. W.; Pron, A. Cu-Fe-S Nanocrystals Exhibiting Tunable Localized Surface Plasmon Resonance in the Visible to NIR Spectral Ranges. *Inorg. Chem.* **2016**, *55*, 6660–6669.
- (16) Lee, S.; Ghosh, S.; Hoyer, C. E.; Liu, H.; Li, X.; Holmberg, V. C. Iron-Content-Dependent, Quasi-Static Dielectric Resonances and Oxidative Transitions in Bornite and Chalcopyrite Copper Iron Sulfide Nanocrystals. *Chem. Mater.* **2021**, *33*, 1821–1831.
- (17) Jain, P. K. Plasmon-in-a-Box: On the Physical Nature of Few-Carrier Plasmon Resonances. *J. Phys. Chem. Lett.* **2014**, *5*, 3112–3119.
- (18) Wang, X.; Swihart, M. T. Controlling the Size, Shape, Phase, Band Gap, and Localized Surface Plasmon Resonance of Cu<sub>2</sub>-xS and Cu<sub>x</sub>In<sub>1-x</sub>S Nanocrystals. *Chem. Mater.* **2015**, *27*, 1786.
- (19) Van Embden, J.; Latham, K.; Duffy, N. W.; Tachibana, Y. Near-Infrared Absorbing Cu<sub>12</sub>Sb<sub>4</sub>S<sub>13</sub> and Cu<sub>3</sub>SbS<sub>4</sub> Nanocrystals: Synthesis, Characterization, and Photoelectrochemistry. *J. Am. Chem. Soc.* **2013**, *135*, 11562–11571.
- (20) Sil, S.; Datta, J.; Das, M.; Jana, R.; Halder, S.; Biswas, A.; Sanyal, D.; Ray, P. P. Bias Dependent Conduction and Relaxation Mechanism Study of CuSFeS<sub>4</sub> Film and Its Significance in Signal Transport Network. *J. Mater. Sci.: Mater. Electron.* **2018**, *29*, S014–S024.
- (21) Mendelsberg, R. J.; Garcia, G.; Milliron, D. J. Extracting Reliable Electronic Properties from Transmission Spectra of Indium Tin Oxide Thin Films and Nanocrystal Films by Careful Application of the Drude Theory. *J. Appl. Phys.* **2012**, *111*, 063515.
- (22) Liu, Z.; Beaulac, R. Nature of the Infrared Transition of Colloidal Indium Nitride Nanocrystals: Nonparabolicity Effects on the Plasmonic Behavior of Doped Semiconductor Nanomaterials. *Chem. Mater.* **2017**, *29*, 7507–7514.
- (23) Marbella, L. E.; Gan, X. Y.; Kaseman, D. C.; Millstone, J. E. Correlating Carrier Density and Emergent Plasmonic Features in Cu<sub>2</sub>XSe Nanoparticles. *Nano Lett.* **2017**, *17*, 2414–2419.
- (24) Conti, C. R., III; Quiroz-Delfi, G.; Schwarck, J. S.; Chen, B.; Strouse, G. F. Carrier Density, Effective Mass, and Nuclear Relaxation Pathways in Plasmonic Sn:In<sub>2</sub>O<sub>3</sub> Nanocrystals. *J. Phys. Chem. C* **2020**, *124*, 28220–28229.
- (25) Conti, C. R.; McBride, J. R.; Strouse, G. F. Examining the Effect of Dopant Ionic Radius on Plasmonic M:ZnO Nanocrystals (M = Al<sup>3+</sup>, Ga<sup>3+</sup>, In<sup>3+</sup>). *J. Phys. Chem. C* **2021**, *125*, 7772–7779.
- (26) Agrawal, A.; Johns, R. W.; Milliron, D. J. Control of Localized Surface Plasmon Resonances in Metal Oxide Nanocrystals. *Annu. Rev. Mater. Res.* **2017**, *47*, 1–31.
- (27) Lounis, S. D.; Runnerstrom, E. L.; Llordés, A.; Milliron, D. J. Defect Chemistry and Plasmon Physics of Colloidal Metal Oxide Nanocrystals. *J. Phys. Chem. Lett.* **2014**, *5*, 1564.
- (28) Goh, S. W.; Buckley, A. N.; Lamb, R. N.; Rosenberg, R. A.; Moran, D. The Oxidation States of Copper and Iron in Mineral Sulfides, and the Oxides Formed on Initial Exposure of Chalcopyrite and Bornite to Air. *Geochim. Cosmochim. Acta* **2006**, *70*, 2210–2228.
- (29) Acres, R. G.; Harmer, S. L.; Beattie, D. A. Synchrotron XPS Studies of Solution Exposed Chalcopyrite, Bornite, and Heterogeneous Chalcopyrite with Bornite. *Int. J. Miner. Process.* **2010**, *94*, 43–51.
- (30) Grosvenor, A. P.; Kobe, B. A.; Biesinger, M. C.; McIntyre, N. S. Investigation of Multiplet Splitting of Fe 2p XPS Spectra and Bonding in Iron Compounds. *Surf. Interface Anal.* **2004**, *36*, 1564–1574.
- (31) Kayaci, F.; Vempati, S.; Donmez, I.; Biyikli, N.; Uyar, T. Role of Zinc Interstitials and Oxygen Vacancies of ZnO in Photocatalysis: A Bottom-up Approach to Control Defect Density. *Nanoscale* **2014**, *6*, 10224–10234.
- (32) Harmer, S. L.; Pratt, A. R.; Nesbitt, H. W.; Fleet, M. E. Reconstruction of Fracture Surfaces on Bornite. *Can. Mineral.* **2005**, *43*, 1619–1630.
- (33) Pratesi, G.; Cipriani, C. Selective Depth Analyses of the Alteration Products of Bornite, Chalcopyrite and Pyrite Performed by XPS, AES, RBS. *Eur. J. Mineral.* **2000**, *12*, 397–409.
- (34) Raeburn, S. P.; Ilton, E. S.; Veblen, D. R. Quantitative Determination of the Oxidation State of Iron in Biotite Using X-Ray Photoelectron Spectroscopy: I. Calibration. *Geochim. Cosmochim. Acta* **1997**, *61*, 4519–4530.
- (35) Sepúlveda, B.; Angelomé, P. C.; Lechuga, L. M.; Liz-Marzán, L. M. LSPR-Based Nanobiosensors. *Nano Today* **2009**, *4*, 244–251.
- (36) Liu, Z.; Zhong, Y.; Shafei, I.; Borman, R.; Jeong, S.; Chen, J.; Losovyj, Y.; Gao, X.; Li, N.; Du, Y.; Sarnello, E.; Li, T.; Su, D.; Ma, W.; Ye, X. Tuning Infrared Plasmon Resonances in Doped Metal-



Oxide Nanocrystals through Cation-Exchange Reactions. *Nat. Commun.* **2019**, *10*, 1394.

(37) Balitskii, O. A. Recent Energy Targeted Applications of Localized Surface Plasmon Resonance Semiconductor Nanocrystals: A Mini-Review. *Mater. Today Energy* **2021**, *20*, 100629.

(38) Ai, K.; Huang, J.; Xiao, Z.; Yang, Y.; Bai, Y.; Peng, J. Localized Surface Plasmon Resonance Properties and Biomedical Applications of Copper Selenide Nanomaterials. *Mater. Today Chem.* **2021**, *20*, 100402.

(39) Ali, M. R. K.; Wu, Y.; El-Sayed, M. A. Gold-Nanoparticle-Assisted Plasmonic Photothermal Therapy Advances Toward Clinical Application. *J. Phys. Chem. C* **2019**, *123*, 15375–15393.

(40) Vines, J. B.; Yoon, J.-H.; Ryu, N.-E.; Lim, D.-J.; Park, H. Gold Nanoparticles for Photothermal Cancer Therapy. *Front. Chem.* **2019**, *7*, 167.

(41) Saeboe, A. M.; Kays, J. C.; Dennis, A. M. Encapsulating Quantum Dots in Lipid-PEG Micelles and Subsequent Copper-Free Click Chemistry Bioconjugation. *Methods Mol. Biol.* **2020**, *2135*, 95–108.

(42) Dubertret, B.; Skourides, P.; Norris, D. J.; Noireaux, V.; Brivanlou, A. H.; Libchaber, A. In Vivo Imaging of Quantum Dots Encapsulated in Phospholipid Micelles. *Science* **2002**, *298*, 1759–1762.